ACS APPLIED MATERIALS & INTERFACES

www.acsami.org Research Article

Freestanding Transparent Organic–Inorganic Mesh E-Tattoo for Breathable Bioelectrical Membranes with Enhanced Capillary-Driven Adhesion

Xiang Li,[§] Junyi Zhang,[§] Bo Shi, Yawen Li, Yanan Wang, Kexiang Shuai, Yue Li, Gege Ming, Tao Song,* Weihua Pei,* and Baoquan Sun*

Cite This: *ACS Appl. Mater. Interfaces* 2025, 17, 22337–22351 Read Online

ACCESS | Metrics & More | Article Recommendations | Supporting Information

ABSTRACT: The electronic tattoo (e-tattoo), a cutting-edge wearable sensor technology adhered to human skin, has garnered significant attention for its potential in brain–computer interfaces (BCIs) and routine health monitoring. Conventionally, flexible substrates with adhesion force on dewy surfaces pursue seamless contact with skin, employing compact airtight substrates, hindering air circulation between skin and the surrounding environment, and compromising long-term wearing comfort. To address these challenges, we have developed a freestanding transparent e-tattoo featuring flexible serpentine mesh bridges with a unique full-breathable multilayer structure. The mesh e-tattoo demonstrates remarkable ductility and air permeability while maintaining robust electronic properties, even after significant mechanical deformation. Furthermore, it exhibits an impressive visible-light transmittance of up to 95%, coupled with a low sheet resistance of 0.268 Ω sq^{-1}, ensuring both optical clarity and electrical efficiency. By increasing the number of menisci between the mesh e-tattoo and the skin, the total adhesion force increases due to the cumulative capillary-driven effect. We also successfully demonstrated high-quality bioelectric signal collections. In particular, the controlling virtual reality (VR) objects using electrooculogram (EOG) signals collected by mesh e-tattoos were achieved to demonstrate their potential for human–computer interactions (HCIs). This freestanding transparent e-tattoo with a fully breathable mesh structure represents a significant advancement in flexible electrodes for bioelectrical signal monitoring applications.

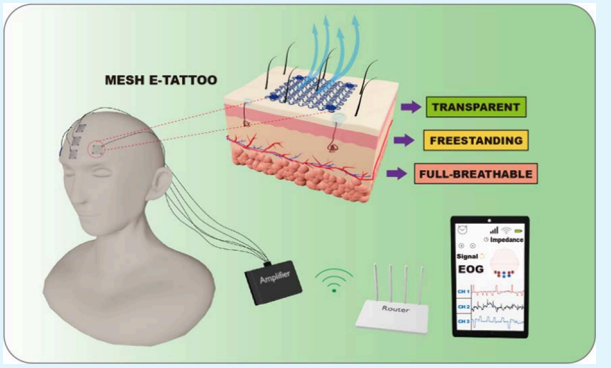

KEYWORDS: *metal mesh, capillary-driven, full breathability, high-transparency, wearable devices*

1. INTRODUCTION

In recent years, the field of brain–computer interfaces (BCIs) has undergone remarkable advancements, implicating a direct connection between the human brain and external devices. BCI technology enables a novel form of interaction by building a bridge between human cognition and machine intelligence.[1] By acquiring and interpreting bioelectrical signals, such as those recorded from electroencephalogram (EEG) electrode arrays placed on human scalps, individuals can control devices and transmit information through their thoughts and intentions.[2] This evolution has ushered in a new era of human–machine convergence.[2−4] Like EEG signals, other bioelectrical signals in humans, including electrocardiogram (ECG), electromyogram (EMG), and electrooculogram (EOG) signals, also provide essential physiological information and are widely utilized in clinical practice.[5] In line with the detection and utilization of physiological details such as sweat[6] and motions,[7,8] these bioelectrical signals are acquired to achieve real-time health monitoring and human–computer interactions (HCIs).[9]

While BCIs demonstrate immense potential, their foundation lies in precisely monitoring biological electrical signals. Currently, the categories of signal acquisition are divided into invasive[10,11] and noninvasive[12] methods. Invasive bioelectrical sensors could collect high-quality electrical signals; however, because of complex medical operations and the risk of inflammation, they are not suitable for daily health monitoring and HCI applications. Noninvasive electrodes, such as dry electrodes made by single-walled nanotubes (SWNTs),[13] silver nanowires (AgNWs),[14] and conductive textiles,[15] wet electro-

Received: January 10, 2025
Revised: February 20, 2025
Accepted: March 26, 2025
Published: April 7, 2025

https://doi.org/10.1021/acsami.5c00565
ACS Appl. Mater. Interfaces 2025, 17, 22337–22351

des like hydrogels[16] have been exploited as essential components of wearable sensors for bioelectrical signal measurements.[17] Typically, noninvasive electrodes record the electrical signal on the surface of human skin. Therefore, the electrodes need to be soft and flexible to meet the mechanical properties of the skin. A dry electrode array was selected for recording facial muscle activity and evaluating the different emotions in face-to-face communications.[18] The adhered dry electrode assisted in recognizing facial features but had a feeble signal quality. Polydimethylsiloxane (PDMS) was laminated on SWNT mesh to form a flexible thin electrode for human physiological monitoring, which showed excellent sensing performance and facile adhesion.[13] Also, PDMS was selected as the substance for fabricating an on-skin flexible electrode by filling silver nanowires in the patterns of the surface, which recorded high-quality EMG signals for detecting diverse force levels of muscles and recognizing hand gestures with decent accuracy.[14] Then, stretchable electronic systems with multilayered high-density integration on organic stretchable fibrous substrates have been reported, achieving stable sensing of bioelectrical signals in wireless communication.[15] In addition, conductive self-adhesive hydrogel electrodes consisting of deep eutectic solvents, waterborne polyurethane, and tannic acid have been reported for the detection of ECGs.[16] These electrodes exhibit clear and precise waveforms with stretchability. However, they are usually bulky with relatively large sizes and thicknesses, which makes it difficult for them to achieve advanced signal recording with a high-density electrode array and discomfortable during prolonged use.[19] Therefore, smaller and thinner skin electrodes are desired for advanced bioelectrical signal monitoring.

Alternatively, the concept of electronic tattoos (e-tattoos), a new form of lightweight wearable electrodes with high precision, high resolution, minimal thickness, and strong adhesion, has emerged as an innovative paradigm in which soft circuits composed of integrated electronic components fixed on flexible substrates are directly adhered to human skin for bioelectrical signal collection. These e-tattoos can be made from elastomers,[20] nanofibers,[21] conductive inks,[22] conductive films,[23] liquid metal,[24] and hydrogels.[25] These e-tattoos offer diverse applications, ranging from biosensing to medical intervention. Owing to the unique characteristics of small size, lightweight, flexibility, and shape-fitting, e-tattoos are considered one of the most promising devices in wearable electronics and HCIs.[26] A multilayered transfer e-tattoo was developed by integrating metal−polymer conductors and an elastomeric block copolymer through a layer-by-layer process.[20] The system could obtain a remarkably amplified output signal with steady contact and a highly stretchable structure. A multifunctional e-tattoo composed of a porous silk nanofiber network functionalized with carbon nanotubes (CNTs) was reported.[21] It allowed accurate monitoring of ECG and EMG signals while monitoring skin temperature and generating heat for therapy with a black-fitting membrane. In addition, an e-tattoo ink with a mixed-dimensional matrix network integrating one-dimensional (1D) cellulose nanofibers/AgNWs and two-dimensional (2D) MXene nanosheets was patterned by printing or direct writing techniques to simultaneously detect human body electrical signals, temperature or humidity variations, and other environmental changes.[22] Similarly, a strategy of printing tattoos on human skin by a direct coating of gallium-based liquid metal with Pt-decorated CNTs was reported.[24] Compared with carbon electrodes, it showed better electrical contact and stable signal acquisition of ECG signals. The dry patterning and wet transferring methods were used to fabricate a patterned e-tattoo of graphene, which showed transparency and conformability to some extent when detecting skin signals with decent signal-to-noise ratios (SNRs).[23] Also, the transferring method was applied to form a tattoo pattern of conductive polymer poly(3,4-ethylenedioxythiophene):poly(styrenesulfonate) (PEDOT:PSS) by transferring it to the skin from the hydrogel layer, which helped to achieve high resolution and conformability for high-quality signal detection.[25] However, the reported e-tattoo strategies so far exhibit compromised breathability and limited transparency due to the visible electronic components and the supporting substrates, which undermines the comfortability and appearance of e-tattoos. These traditional e-tattoos with substrates or thick visible electronic components hinder the natural permeability and breathability of skin and result in noticeable colors and shapes when someone is wearing them on exposed areas of the human body, such as the face, neck, and hands. Therefore, fully breathable freestanding transparent e-tattoos are highly required for bioelectrical signal collection in daily life. These challenges in developing advanced e-tattoos stem from rational device structure design and careful selection of functional materials.

To address these issues, we proposed a freestanding transparent e-tattoo featuring a flexible and deformation-tolerant serpentine structure that comprises a conductive metal mesh skeleton integrated with a biocompatible soft conductive polymer coating layer. The serpentine mesh structure offers remarkable mechanical flexibility, stretchability, and malleability. The grid mesh structure was constructed with a line width as thin as ∼15 μm to meet the requirements of invisibility, stretchability, air breathability, and high-quality signal recording. The e-tattoo consists of periodical mesh bridges with a unique full-breathable multilayer mesh structure. According to theoretical calculations, increasing the number of bridge menisci could enhance the total metal grid-electrode adhesion force on skins due to the cumulative capillary-driven effect of each meniscus. The mold used to shape the mesh pattern was fabricated using photolithography, which allowed us to create microscale photoresist trenches with precise dimensions on an indium tin oxide (ITO) substrate. Nickel (Ni) was chosen as the material for the conductive mesh skeleton due to its inherent stability and conductivity. To enhance the ductility of the pure Ni mesh, which is prone to snapping, we chose gold (Au) as the coating layer. Additionally, to improve the electrical contact between metal and skin, we applied a conductive polymer of doped poly(3,4-ethylenedioxythiophene) (PEDOT) on the outermost surface of the metal mesh. PEDOT provides excellent electrical interface compatibility that closely matches the electrical and mechanical conditions of the skin. Also, the introduced perchlorate in the electrochemical process assists in adjusting the charges of doped PEDOT, promoting hydrophilicity, which plays an important role in wettable adhesion. Furthermore, the special structure with ultrathin mesh lines offers exceptional transparency and gas permeability, making it suitable for daily bioelectrical signal recording on exposed skin such as faces and necks. Our breathable and transparent mesh e-tattoos represent a novel approach for realizing continuous monitoring of human bioelectrical signals. Their unique design and

https://doi.org/10.1021/acsami.5c00565
ACS Appl. Mater. Interfaces 2025, 17, 22337−22351

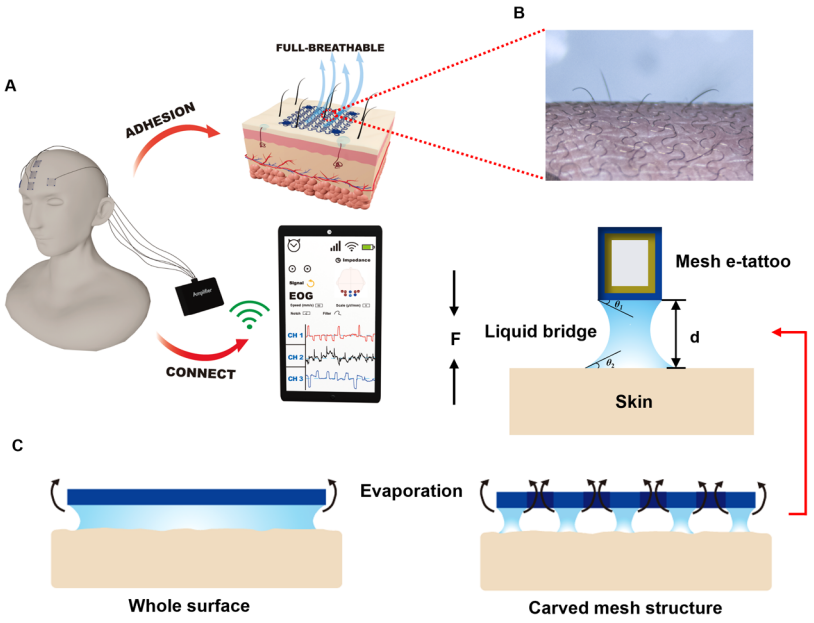

Figure 1. Schematic illustration of the adhesion condition and fabrication of the PEDOT-coated Au@Ni mesh e-tattoo. (A) Diagram of the attachment and data transmission of mesh e-tattoo. (B) Digital photograph of mesh tattoo on skin. (C) Schematic diagram of adhesion by the water of the whole surface of PEDOT/Au/Ni and PEDOT-coated Au@Ni mesh e-tattoo, and the detailed schematic of the meniscus force between mesh and skin with the function of liquid bridge. The force is generated by the liquid surface tension within the menisci. When liquid adsorbs, the formed liquid bridge will create interactions between two surfaces.

material composition offer significant potential in the field of wearable sensors for HCIs.

2. RESULTS AND DISCUSSION

2.1. Design and Fabrication of Freestanding Mesh E-Tattoos. A freestanding flexible e-tattoo was designed and developed for monitoring human bioelectrical signals, which was composed of a serpentine mesh and round electrical contacts at four corners (Figure S1). The mesh e-tattoo can adhere to skin conformingly with full breathability, where fine hairs stretch out from the mesh voids (Figure 1A). The actual condition of skin-mesh adhesion is shown in Figure 1B, indicating a delicate attachment between the two surfaces. When the polymer layer comes into contact with human skin, the surface tension of sweat driven by the capillary force aids in the vertical adhesion between two surfaces along with electrical conductivity. In the biological attachment systems in nature, such as those found in geckos' feet, the splitting of one large liquid bridge contact element ($N = 1 \times 1$) into numerous smaller, hairlike elements ($N = n \times n$) could effectively enlarge the adhesion force on flat surfaces.[27] The benefits of this contact-splitting principle include an increase in the capillary adhesion force proportional to the number of contacts. Provided that two hydrophilic surfaces contact each other by a liquid bridge, two types of forces come into play: meniscus force and viscosity force.[28] The meniscus force, driven by the Laplace pressure generated by the liquid surface tension within the menisci, contributes to the attraction between the surfaces. This force is influenced by contact angles and the separation distance, which can be quantified using the eq 1 below:

$$F_m = \frac{\pi R^2 \gamma(\cos\theta_1 + \cos\theta_2)}{d} + 2\pi\gamma R \sin\theta_{1,2} \quad (1)$$

where R is the radius of the meniscus, γ is the surface tension of liquid, d is the distance between surfaces, and $\theta_{1,2}$ is the contact angle of liquid on two surfaces. According to the equation, the meniscus force is enhanced with the decline of separated distance. On the other hand, the viscosity force comes from the viscosity of liquid when a transient separation between two surfaces occurs, which exhibited a remarkable rise by increasing separated distance until the breaking point. The eq 2 for viscosity force is shown as

$$F_v = \frac{3\pi\eta R^4}{4t}\left(\frac{1}{d_s^2} - \frac{1}{d_0^2}\right) \quad (2)$$

where η is the kinematic viscosity of the liquid, t is the separating time, d_s is the distance at the breaking point, and d_0 is the initial distance. Since the viscosity force is related to the separating rate, whereas the e-tattoo adhesion is static, the viscosity force was not taken into account in the attaching condition of e-tattoos. In the contact angle test, the average contact angle on the doped PEDOT surface was ~56°, while the value on the skin was ~75° (Figure S2), respectively. The surface tension of water is approximately 71.97 mN/m, and assuming a separation distance of 0.2 mm, we can estimate the meniscus force for different surface structures. For a compact PEDOT surface ($N = 1 \times 1$) with dimensions of approximately 1.4 cm × 1.4 cm, the extracted meniscus force was around 97.10 mN. However, in the case of a carved mesh structure, the size of each meniscus is limited by the width of the grids. Therefore, the overall adhesion can be viewed as the cumulative effect of multiple menisci. To calculate the total meniscus force for a $2R \times 2R$ flat surface with $N = n \times n$ menisci (Figure S3), we can use eq 3:

$$F_{m,total} = NF_m\left(\frac{R}{n}\right) \quad (3)$$

where R/n is the radius of every sphere (whole mesh cross section) with the meniscus, F_m can be calculated using eq 1. Through calculation, the carved structure occupied ~5% of the

https://doi.org/10.1021/acsami.5c00565
ACS Appl. Mater. Interfaces 2025, 17, 22337−22351

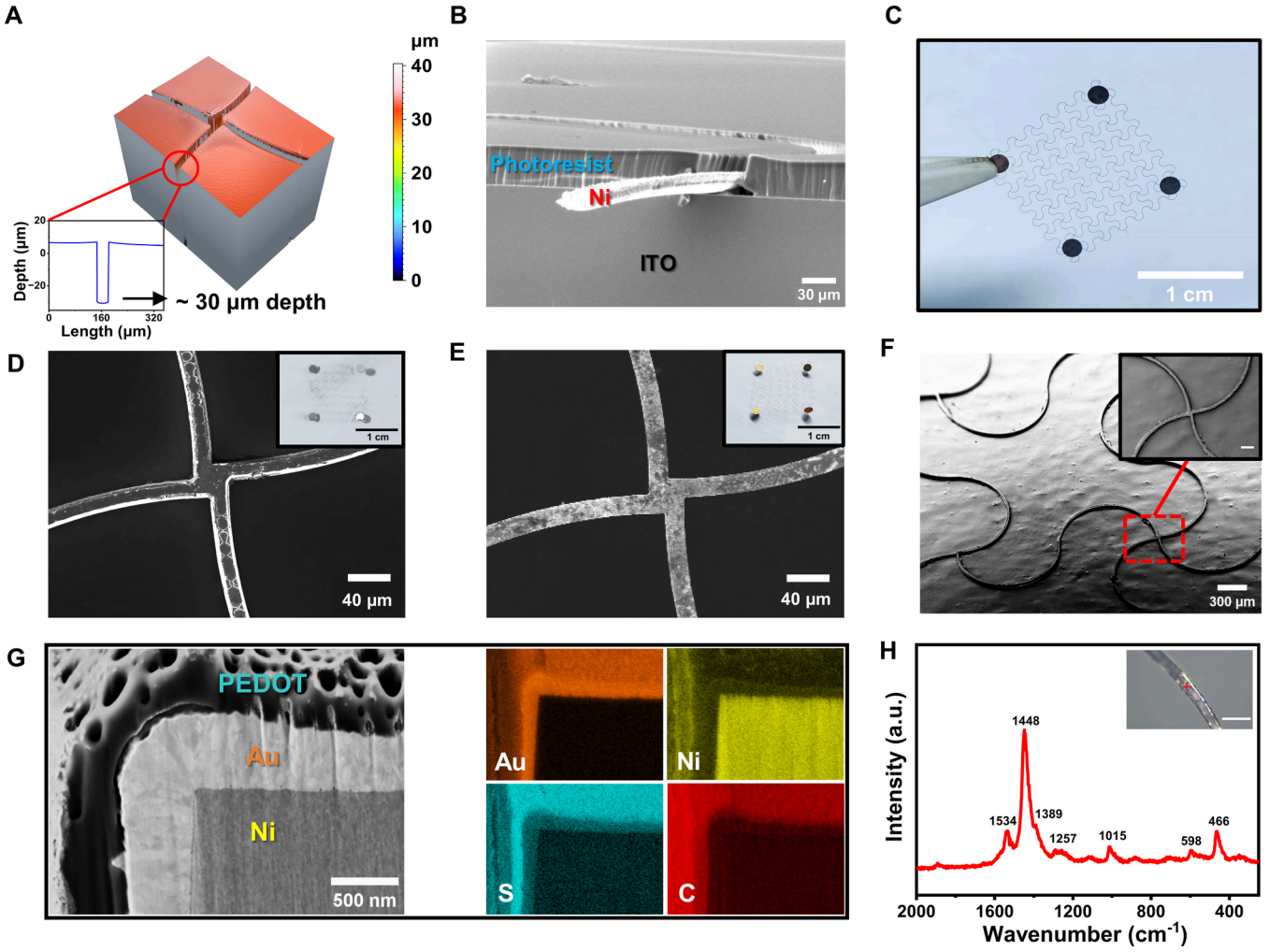

Figure 2. Freestanding flexible mesh e-tattoo appearance. (A) 3D image of the mesh pattern after photolithography (approximately 30 μm depth). (B) SEM image of the photoresist pattern profile with deposited Ni. (C) Digital photographs of the mesh e-tattoo, which shows an ultrathin line width. The dimensional size of the whole e-tattoo was ~1.4 cm × 1.4 cm. (D) SEM image of the pure Ni mesh. The inset shows the entire Ni mesh region. (E) SEM image of the Au@Ni mesh. The inset shows the whole Au@Ni mesh region. (F) SEM image of the PEDOT-coated flexible mesh e-tattoo. The inset shows the zoom-in part of the mesh e-tattoo (scale bar of the inset image: 100 μm). G) Cross-section of the mesh e-tattoo and the main elements distribution (Au, S, Ni, and C). (H) Raman spectrum of the mesh e-tattoo surface with an excitation wavelength of 633 nm. The inset shows the zoom-in mesh grid (scale bar of the inset image: 40 μm).

whole area. Thus, $N \times 5\%$ was set as the sum. The number of each side, n_1, could be regarded as $(1/2\sqrt{5})\ n$. So, the expression (eq 4) of meniscus force for the mesh structure could be written as

$$F_{m,mesh} = \frac{\sqrt{5}}{10} N F_m \left(\frac{R}{n}\right) \tag{4}$$

where $2R$ is ~14 mm, R/n is ~7.5 μm for the mesh. The meniscus force on the PEDOT surface of the mesh tattoo was calculated to be approximately 141.85 mN. This force is about 1.5 times stronger than the force generated by PEDOT covering the entire surface. Additionally, the voids in the mesh structure contribute to the evaporation of water. This evaporation helps to reduce the separation distance between the mesh and the skin, resulting in a meniscus force larger than that of a solid surface over the same time interval. The evaporation effect not only improves adhesion but also aids in maintaining a strong meniscus force over time. Overall, the carved design of the mesh tattoo offers improved adhesion when compared to a compact surface, especially in sweaty conditions, due to the combined effects of increased meniscus force and water evaporation (Figure 1C).

In Figure S4, a schematic illustration of the detailed fabrication process is depicted. Typically, the whole process begins with cleaning ITO substrates and spin-coating the photoresist. To improve the thickness and stability of the pattern mold in chemical solvents, the negative photoresist SU-8 was chosen due to its excellent resolution and chemical resistance. Considering the strong attachment of the SU-8 photoresist on ITO substrates, a spin-coated OmniCoat layer was introduced as a sacrificial layer between the substrate and the photoresist to assist the stripping process. Then, we transferred the serpentine mesh pattern onto the ITO substrates by photolithography. After the developing procedure, the substrates were subjected to oxygen plasma to remove the residual OmniCoat layer at the bottom of the serpentine trench. Subsequently, we immersed the substrates in Ni sulfate electroplating solution, which was connected to the cathode of the electroplating power supply, while the anode was connected to one piece of a Ni plate. Ni metal mesh

https://doi.org/10.1021/acsami.5c00565
ACS Appl. Mater. Interfaces 2025, 17, 22337−22351

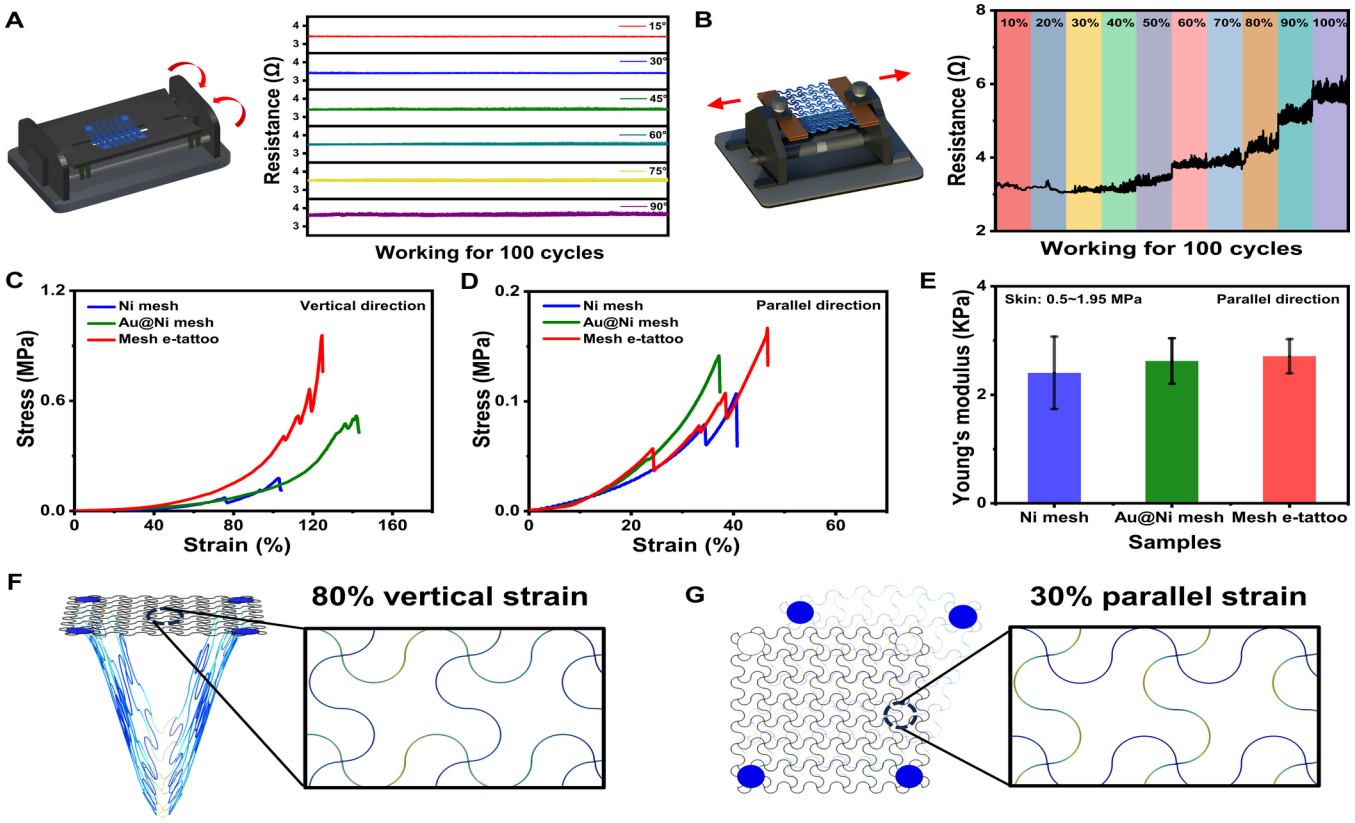

Figure 3. Mechanical characterization of mesh e-tattoo. (A) Resistance change in the repeated bending process from 15 to 90° for 100 cycles. The corresponding radii of curvature are ~2.78, ~3.06, ~3.40, ~3.82, ~4.37, and ~5.09 (mm) from 15 to 90°, respectively. (B) Resistance change in the repeated stretching process from 10 to 100% for 100 cycles. (C) Force−displacement plots of Ni mesh, Au@Ni mesh, and mesh e-tattoo in the vertical three-point bending test. (D) Force−displacement plots of three types of samples in the parallel stretching test. (E) Young's modulus comparison of three types of samples in a parallel stretching test. The inset also provides human skin with Young's modulus value of 0.5−1.95 MPa. FEA simulation analysis of the mesh e-tattoo when withstanding (F) 80% deformation in the conditions of vertical strain and (G) 30% deformation of parallel strain.

was deposited in the serpentine trench of the photoresist pattern on conductive ITO substrates to form the conductive skeleton. In the following step, the substrates were soaked in *N*-methyl pyrrolidone at 50 °C to strip the photoresist and OmniCoat layer to release the freestanding Ni mesh. Ni mesh was fabricated as the skeleton because of its self-supportability conductivity. Moreover, a thin layer of Au was coated on the freestanding Ni mesh through a similar electrodeposition method to promote the ductility. The final step was the electrical polymerization of PEDOT on the freestanding metal mesh as a conductive interfacial layer to enhance the electrical contact between the e-tattoo and human skin. Before electropolymerization, the mesh was modified by amino groups and the subsequent poly(vinyl alcohol) (PVA) adhesive layer to prevent the polymer from detaching from the metal surface.[29] Concerning the fact that the mesh structures were constructed by ultrathin line widths, dip coating or spin coating is inapplicable for conformal coating of the PEDOT layer due to the effect of capillary forces. Consequently, electropolymerization is an effective strategy for conductive polymers such as PEDOT to form conformal coatings attached to mesh lines instead of accumulating the conducting polymer in the voids of the mesh, finally preserving the air permeability and decreasing the contact resistance at the same time. The detailed electrodeposition reaction equations are illustrated in the Supporting Information.

The origin depth of the photoresist trench was ~30 μm, according to the confocal microscopy image (Figure 2A). After Ni deposition, the trench was partially filled with Ni with a thickness of ~20 μm (Figure 2B). After depositing the Au and PEDOT layers on a freestanding Ni skeleton, the completed mesh e-tattoo could be suspended by a tweezer, demonstrating novel self-supportability (Figure 2C). As shown in the scanning electron microscopy (SEM) images, the coverage of the Au and PEDOT coating layer on the Ni mesh was uniform and conformal. The deposition of Au coating promoted smoothness, and the subsequent PEDOT coat made the surface coarser and softer (Figure 2D−F). The conductive polymer coating contributed to human skin adhesion due to the much smaller mechanical modulus compared to those of common metals.[30] We also attempted cheaper metal Cu as a shell layer on the Ni skeleton instead of Au to cut down the fabrication cost. However, the Cu@Ni mesh exhibited poorer stability than Au ones when detecting bioelectrical signals due to the electrochemical activity of Cu.[31] As shown in Figure S5, the signals from the Cu mesh presented inferior stability. Accordingly, Au was finally chosen as the coating layer. Cross-section SEM image and electron-dispersive spectroscopy (EDS) mappings revealed the main element distribution in the triple-layer structure (Figure 2G). The thicknesses of Au and the PEDOT shell were ~500 and ~300 nm, respectively. The Au layer was designed to coat the Ni skeleton uniformly. A thinner Au layer of ~50 nm had been deposited and revealed

https://doi.org/10.1021/acsami.5c00565
ACS Appl. Mater. Interfaces 2025, 17, 22337−22351

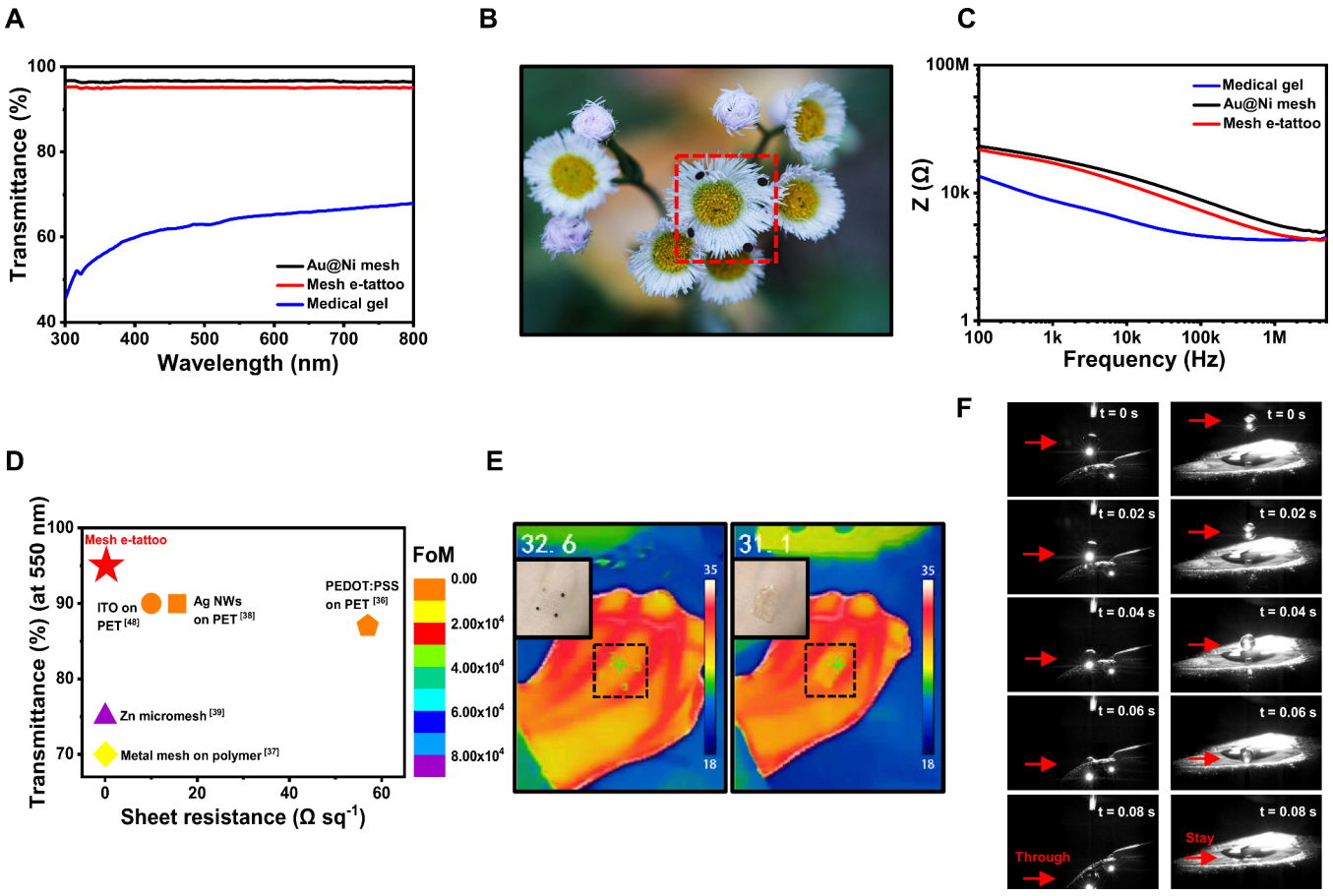

Figure 4. Optical and electrical properties of the mesh e-tattoo. (A) Transmittance of Au@Ni mesh, medical gel, and mesh e-tattoo in the visible-light wavelength range. (B) Digital photograph of the mesh e-tattoo put on a chrysanthemum flower in the natural environment. (C) Impedance–frequency plots for samples of the mesh e-tattoo, Au@Ni mesh, and medical gel attached to human skin. (D) Figure of transmittance (at 550 nm)–sheet resistance for typical transparent electrodes. The corresponding FoM is marked with different colors. (E) Infrared thermal images of medical gel and mesh e-tattoo attached on the hand back. The insets show the photo in the black dash line region. (F) Process of a water drop falling on the surfaces of mesh e-tattoo (left) and medical gel (right).

poor coverage on Ni mesh (Figure S6). In addition, the Raman spectrum of e-tattoo was collected at an excitation wavelength of 633 nm to identify the structure of the electrical polymerized PEDOT layer (Figure 2H). The main peaks were located at 1534 cm^{-1} (symmetric C_β–C_β stretching vibrations), 1448 cm^{-1} (thiophene ring, symmetric C_α=C_β stretching vibrations), and 1389 cm^{-1} (C_β–C_β stretching vibrations), while the weaker peaks were located at 1257 cm^{-1} (C_α–C_α' inter-ring stretching vibrations), 1015 cm^{-1} (oxyethylene ring deformation), 598 cm^{-1} (oxyethylene ring deformation), and 466 cm^{-1} (C–O–C deformation), which were lined well with the PEDOT Raman signal.[32]

2.2. Mechanical Properties of Mesh E-Tattoos. To explore the mechanical strength of the mesh e-tattoo after long-term wear, we detected the electrical resistance changes at the two ends during the process of repeated folding and stretching of the e-tattoo to different extents. Figure 3A shows repeated folds between 15 and 90° with a 15° gradient for 100 cycles. From the process of 15 to 90° folding, the range of resistance varied slightly but remained stable over the whole measurement. The original resistance of a flat e-tattoo was 3.4 Ω. Under folded conditions, the resistance fluctuated between 3 Ω and 4 Ω, with a minimum value of approximately 3.4 Ω (15° folding) and a maximum value of approximately 3.7 Ω (90° folding) (Figure S7). Even after being folded to 90°, the mesh e-tattoo still showed decent conductivity and experienced little change in shape. Similarly, 10 to 100% stretching was applied with a 10% extending stretching step gradient (Figure 3B). In the figure, various stretching ranges are represented by different background colors. For each stretching step condition, the stretching–relaxing cycle was repeated 100 times. Through a continuous measurement, the resistance was found to change from an initial 3.4 to approximately 6.3 Ω after 100% stretching for 100 cycles. The final resistance after 100% stretching was slightly higher than that of the 90° folded sample. Several steep rises of resistance could be observed in the case of 60, 80, 90, and 100% stretching, corresponding to the partial breakage of the mesh structure. When stretched to 100% of the original length, the mesh e-tattoo was nearly fractured, but the e-tattoo still showed decent resistance, which was only approximately doubled compared with that of a freshly prepared device, suggesting impressive durability and robust resistance. In a real bioelectrical signal collection scenario, the tattoo could continue operating even when partially cracked or snapped, which benefited from the highly conductive serpentine metal mesh structure. Figure S8 exhibits photographs when the sample was stretched to 100%, which showed the remaining mesh lines for electrical signal transport. Long-term mechanical deformation tests revealed that the electrical properties of the

https://doi.org/10.1021/acsami.5c00565
ACS Appl. Mater. Interfaces 2025, 17, 22337–22351

mesh e-tattoo stayed robust against copious shape deformation processes. Table S1 summarizes the resistance variations of some common transparent conductive electrodes (TCEs) after deformation, where the mesh e-tattoo exhibited excellent performance.[33,34]

Then, the deformation limit was measured by vertical stretching in the middle (three-point bending test) and parallel stretching from one side (Figure 3C,D). The winding upward trends of plots are attributed to random cracks of grid lines in the process of stretching (Figure S9). During vertical stretching, the Ni skeleton mesh exhibited obvious breakage at approximately 40% strain, while the Au@Ni mesh and the e-tattoo experienced breakage at approximately 50% strain. With increasing mesh thickness, the force at the yield point applied to the samples was ∼0.2 MPa for the Ni mesh, ∼0.5 MPa for the Au@Ni mesh, and ∼0.9 MPa for the Au@Ni@PEDOT mesh e-tattoo. This trend indicated an improvement in flexibility after coating with the Au and PEDOT layers. According to the results of the parallel stretching test, the e-tattoo could withstand a higher strain of ∼50% compared with those of the bare Ni skeleton and Au@Ni mesh. The related stresses were gradually changed to approximately 0.1 MPa for the Ni mesh, 0.14 MPa for the Au@Ni mesh, and 0.17 MPa for the Au@Ni@PEDOT mesh e-tattoo, indicating improved stretchability. Figure 3E depicts the values of Young's modulus for the parallel stretching test of the three samples. The calculated moduli were ∼2.40 kPa for the pure Ni mesh, ∼2.62 kPa for the Au@Ni mesh, and ∼2.71 kPa for the Au@Ni@PEDOT mesh e-tattoo, respectively. The Young's modulus was slightly promoted with Au and PEDOT coating, but the samples still exhibited excellent flexibility, which is much lower than the modulus of human skin (approximately 0.5−1.95 MPa[35]).

Moreover, finite element analysis (FEA) was used to assess the theoretical mechanical behavior of the Ni mesh skeleton, while it was being stretched to the point of breakage. The 80% strain of vertical stretching and 30% strain of parallel stretching were simulated by FEA, where the grids had begun to break at the stretching ratios according to the mechanical test. Specially, in parallel stretching, when the 40% tensile test was applied, the mesh was stretched out of shape with severely deformed mesh lines, which indicated nearly complete breakage. In repeated stretching tests, the value of resistance only increased by ∼9% after long-time stretching. This discrepancy in the results of repeated stretching tests could result from the properties of the mesh structure, which was conductive, even though only a few lines were connected. In terms of the geometry of the serpentine structure, the mesh e-tattoo was more tolerant of stretching than common straight-line meshes were.[34]

2.3. Optical, Electrical, and Breathable Characteristics. Figure 4A exhibits the excellent optical transparency of the mesh e-tattoo. For the Au@Ni mesh, the value reached 96% for visible light. After the electropolymerization of PEDOT on mesh, the light transmittance of mesh e-tattoo only exhibited an approximately 1% decline to ∼95%. The commercial medical gel was also used as a reference. The transmittance of medical gel was ∼65% at 550 nm with a rising trend with the wavelength, while mesh e-tattoo presented neutral light transparency in the full visible-light spectrum range. The high transparency of the mesh e-tattoo could be attributed to the ultrathin line width (approximately 15 μm) and the absence of a supporting substrate. The denser mesh e-tattoo with 36 × 36 grid lines was also fabricated, whose light transmittance was approximately 63%, which was ∼32% lower than the original mesh (Figure S10). The performance of these materials exceeded that of similar flexible transparent electrodes with high transmittance.[36−39] Also, the haze of mesh e-tattoo was measured (0.656−1.266%), which is comparable with normal glass (0.2−0.8%),[40] as shown in Figure S11. The photograph of a mesh e-tattoo covered on a flower in the natural environment demonstrated its enchanting light transparency (Figure 4B).

In addition, the contact impedances of the Ag/AgCl medical gel, the Au@Ni mesh, and the e-tattoo were measured to explore the quality of electrical contact of the mesh e-tattoo on human skin (Figure 4C). The plots of all of the samples exhibited falling trends with increasing frequency from 100 Hz to 5 MHz. We also measured the impedance of the samples from 1 to 100 Hz, which showed the same trend and acceptable resistance values (Figure S12). The results exhibited the adaptability of the mesh e-tattoo in the signal range of 1 Hz−5 MHz, covering the working frequency range of common bioelectrical signal detection.[41] As Figure 4C shows, the contact resistances of the Au@Ni mesh, the Au@Ni@PEDOT mesh e-tattoo, and the medical gel at 100 Hz were ∼295, ∼230, and ∼34 kΩ, respectively. The measurement of contact impedance was repeated in response to different air humidities and various skin conditions. For all of the measurements, the impedance values generally followed the trend and remained below 300 kΩ. Upon coating with PEDOT, the reduced contact resistance demonstrated enhanced surface adhesion and electrical contact with skin, potentially benefiting from improved interfacial contact. On the one hand, the grained rough surface of polymerized coating adapts to wrinkled skin. On the other hand, in each EDOT molecule, there are two oxygen and one sulfur atom, which can enhance its *van de Waals* force and hydrogen bond with the dewy epidermis[42−44] (Figure S13). In addition, the mixed electronic/ionic conduction of PEDOT assists in abating electrochemical impedance.[45] When skin perspires, the ions in sweat flow to the skin surface, which assists the ion transfer and promotes the capacitive process between skin and PEDOT.[46]

The figure of merit (FoM) was extracted to evaluate the optical and electrical properties. This metric indicates the ratio of electrical impedance to optical transmittance and is usually used for estimating TCEs. The specific relationship can be calculated using $\mathrm{FoM} = \frac{188.5}{R_s\left(\frac{1}{\sqrt{T}} - 1\right)}$[34,47] where T represents the transmittance at a wavelength of 550 nm and R_s represents the sheet resistance of the transparent electrode. The sheet resistance of the mesh e-tattoo was ∼0.268 Ω sq^{-1}, which was directly measured and averaged by a four-probe resistance meter. The low resistance can be attributed to the conductive metal skeleton. Figure 4D shows the FoM values of several typical conductive films or meshes. The schematic diagram demonstrates the superior transparency and low sheet resistance of the mesh e-tattoo with the FoM value up to 2.7 × 10^4, whereas it was 348 for ITO on PET (90%, 10 Ω sq^{-1}),[48] 46 for PEDOT:PSS on PET (87%, 57 Ω sq^{-1}),[36] 1.5 × 10^4 for the metal mesh on polymer (70%, 0.07 Ω sq^{-1}),[37] 223 for Ag NWs on PET (90%, 15.6 Ω sq^{-1}),[38] and 8.5 × 10^4 for the freestanding Zn micromesh electrode (75%, 0.015 Ω sq^{-1}).[39] Note that the Zn micromesh illustrated a high value of FoM, but the transmittance of 75% was much lower than ∼95% of our mesh e-tattoo.

https://doi.org/10.1021/acsami.5c00565
ACS Appl. Mater. Interfaces 2025, 17, 22337−22351

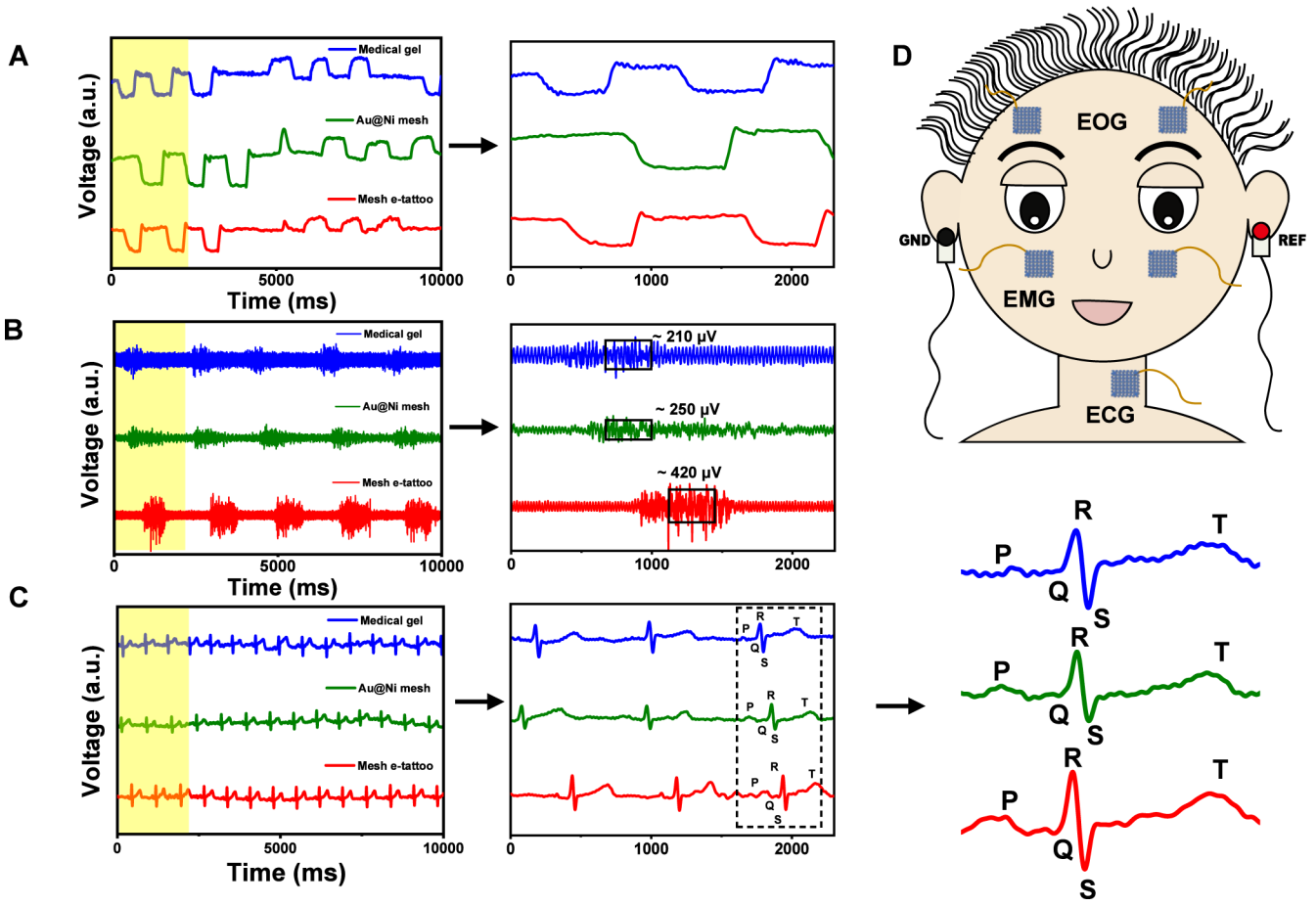

Figure 5. Schematic illustration of signal detection and comparisons. (A) EOG signals of "look left" and "look right" three times in sequence, recorded with medical gel, Au@Ni mesh, and mesh e-tattoo bioelectrodes. The right image shows the enlarged data from 0 to 2.3 s in the beginning, marked with a yellow background. (B) EMGs of zygomaticus detected with three types of electrodes during a smiling face/no facial expression for five times. The right image shows the enlarged data from 0 to 2.3 s in the beginning, marked with a yellow background. (C) ECG signals collected in 10 s. The middle image shows the enlarged data from 0 to 2.3 s in the beginning, marked with a yellow background. A single waveform of each electrode is further zoomed in to show the characteristics P, Q, R, S, and T peaks in ECG. (D) Schematic diagram of bioelectrical signal detection, illustrating the position of attached electrodes for EOG, EMG, and ECG measurements.

To reveal the performance of the mesh e-tattoo in terms of breathability, a tattoo sample and a piece of medical gel with similar size and shape were adhered to a human hand for comparison. An infrared thermal image camera was utilized to probe the overall temperature distributions for the two samples on hands. From Figure 4E, an abrupt temperature change was detected between the medical gel-covered area and the surrounding bare skin area. The temperature in the medical gel-covered area was 31.1 °C, while the temperature of uncovered hand skin was around 35.0 °C. However, the skin covered by the mesh e-tattoo maintained a uniform temperature distribution (around 32.6 °C for the whole area) without an obvious temperature change to the hand skin, which demonstrated the omittable thermal effect of the mesh e-tattoo on the skin. Only the four round electrical contact pads (with a radius of 1 mm) were observable. Furthermore, as shown in Figure 4F, water drops could pass through the mesh e-tattoo freely, showing superior water and gas permeability. In comparison, water drops were preserved on the surface of the medical gel patch due to its poor breathability.

We explored the electrical contact stability of mesh e-tattoos on the skin. During a long-term test, the impedance change with time has been detected on a piece of pig skin for 7 days, where the value did not change significantly. The impedance of the medical gel on pig skin was also tested for comparison, which showed an obvious increase while the mesh e-tattoo remained stable during 8 h (Figure S14). Furthermore, a mesh e-tattoo sample and a medical gel were affixed to human skin for 12 h. Both skin conditions and contact impedance were monitored at the start and end of the test (Figure S15). Initially, the contact impedance of the mesh e-tattoo was approximately 283 kΩ, whereas the medical gel exhibited a lower value of ∼205 kΩ. However, after 12 h, the e-tattoo impedance had significantly decreased to ∼67 kΩ, while the medical gel impedance only fell to ∼114 kΩ. After 12 h of attachment, the decline in the contact impedances of both electrodes likely stemmed from sweat or salt secreted by the skin during daily activities, while the plunge of the mesh e-tattoo indicated a more intimate contact through accelerated sweat evaporation. Moreover, the salt in sweat may also boost the ion conductivity of the PEDOT layers. Photographs taken after removal of both electrodes after 12 h revealed that the mesh e-tattoo caused minimal, if any, skin discomfort even after prolonged wear, whereas the medical gel caused slight skin allergic reactions.

https://doi.org/10.1021/acsami.5c00565
ACS Appl. Mater. Interfaces 2025, 17, 22337−22351

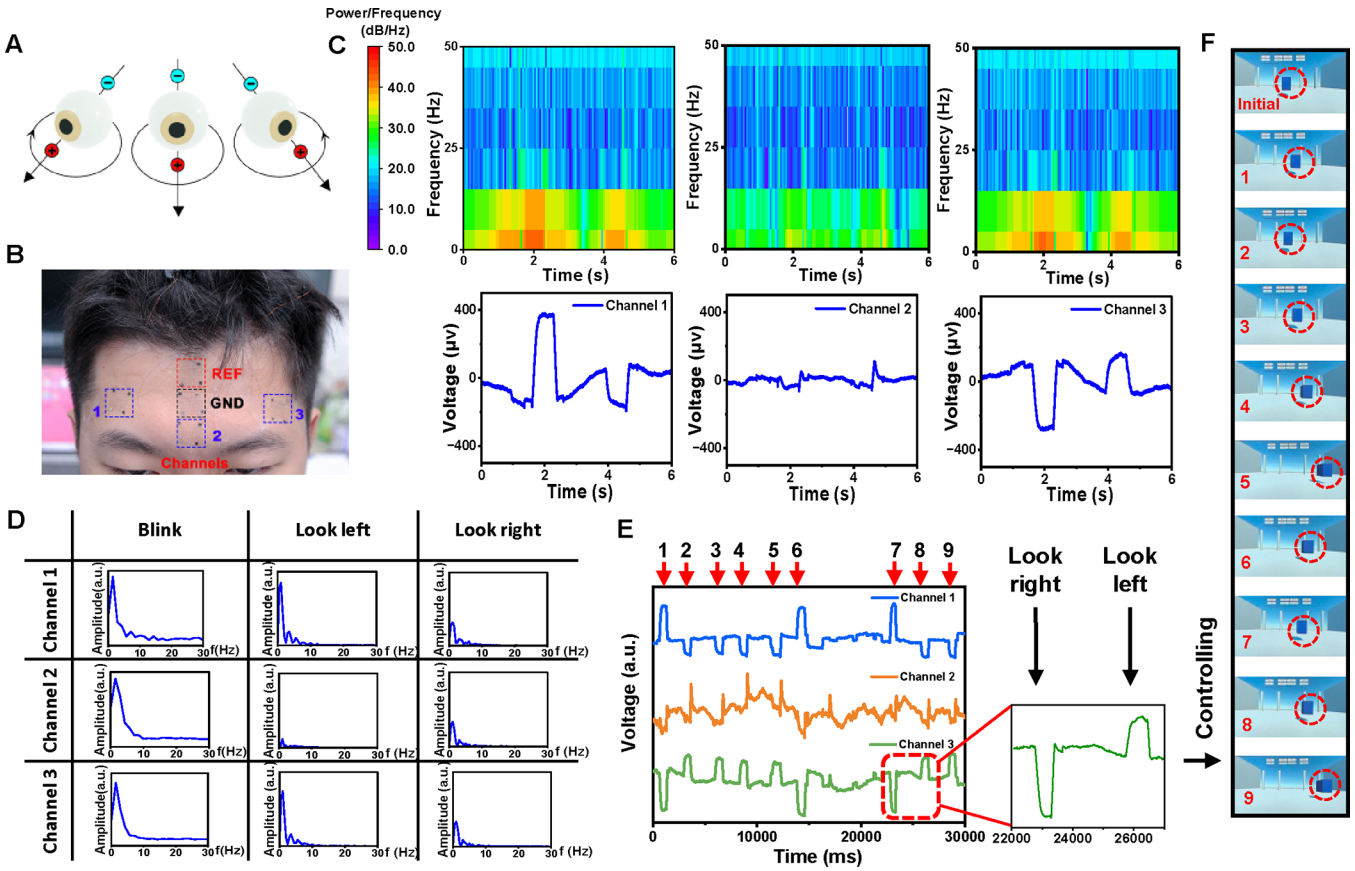

Figure 6. Real-time EOG detection and interaction with VR. (A) Schematic diagram of ocular potential changes with eye movements. (B) Illustration of the positions of mesh e-tattoos attached to the forehead for EOG detection. (C) Time–frequency plot (above) of signal power for the corresponding EOG signal (below) derived from the mesh e-tattoo electrodes. Figures of amplitude-frequency change with time by short-time Fourier transform (STFT) analysis (top) and main EOG signals. (D) Amplitude–frequency plots of EOG signals for the events of "blink", "look left", and "look right" analyzed by the fast Fourier transform (FFT) method. (E) Real-time EOG detection for HCI demonstration of (F) controlling the movements of an object in a VR environment.

2.4. EOG, ECG, EMG Signal Monitoring and HCI Applications. Typical bioelectrical signals are generated because of electrical potential differences that come from the flow of ions through the cell membrane.[49] To test the feasibility of the mesh e-tattoo in bioelectrical signal monitoring, we collected EMG and ECG signals with wet medical gel, Au@Ni mesh, and mesh e-tattoo, separately for comparison. The collected bioelectrical data and the schematic graph illustrating the position of adhered electrodes on the human face are shown in Figure 5. The EOC, EMG, and ECG signals were collected at the forehead, the zygomaticus major muscles, and the carotid artery on the neck, respectively, as depicted in Figure 5D. The EOG signals detected by the three types of electrodes are displayed in Figure 5A, corresponding to the eye movement of looking left and right three times. The medical gel was used as a standard reference, and the working electrode was adhered on the forehead above the eyes. Compared with medical gel, the mesh e-tattoo produced slightly enhanced signal quality, where the nearly straight baseline of eye movement could be monitored, showing smaller fluctuations. Meanwhile, the electrical signal detected by Au@Ni mesh electrodes was affected by a drifting baseline, while the Au@Ni@PEDOT mesh e-tattoo provided a stable plain baseline, indicating that the conductive polymer coating facilitated bioelectrical signal transfer across the electrode/skin interface.

Figure 5B depicts the EMG signals when smiling and no facial expression, collected by attaching the electrodes on the human face where the zygomatic major muscles locate. After the signals were filtered by MATLAB with the same processes to eliminate environmental factors, we assessed the ratio of intensity between signal peaks and baseline noise. EMG signals with average levels of ∼210, ∼250, and ∼420 μV were recorded with medical gel, Au@Ni mesh, and mesh e-tattoo, respectively, while the baseline noise obtained by Au@Ni mesh and mesh e-tattoo electrodes (∼100 μV) was only half of the noise level obtained by medical gel (∼200 μV). The SNR value showed that the mesh e-tattoo (15.78 dB) had a better performance than the Au@Ni mesh (14.86 dB), whereas it was slightly lower than commercial medical gel (18.13 dB). Also, the SNR values of the other two signals were calculated (Table S2), and the same trend was observed. This opposite consequence with measured impedance should be assigned to the following factors. First, the gel electrode displayed a larger contact area than the mesh electrode, which was more sensitive and susceptible to interference from other muscles. Second, the motion artifact produced by muscle wrinkles in long-time wear.[50] Finally, compact contact was realized between mesh electrodes and skin, while gel electrode attachment was influenced by fine hair on the human body (Figure S16). We have taken the 3D height images of the mesh e-tattoo attached to pig skin with a 3D confocal microscope

https://doi.org/10.1021/acsami.5c00565
ACS Appl. Mater. Interfaces 2025, 17, 22337−22351

(Figure S17). The step height from the top surface of the mesh e-tattoo to the surface of the pig skin was ∼20 μm, which is consistent with the thickness of the mesh e-tattoo, indicating the seamless and conformal contact between the mesh e-tattoo and pig skin. The pronounced EMG signal intensity and low baseline noise level observed by the mesh e-tattoo resulted in a better SNR for high-quality EMG signal recording.[51]

Additionally, ECGs were collected by attaching electrodes near the carotid artery on the neck (Figure 5C). The ECG curves recorded by these three electrodes exhibited clear and smooth waveforms. According to the zoomed ECG data, the signal collected by medical gel was relatively lower and slightly influenced by random electrical noise, while the mesh e-tattoo collected the strongest signals with minimal noise affection. The intensity ratio of P and R peaks was calculated to evaluate the quality of ECG, where a larger value represented a clearer P wave in the detecting process, avoiding the misjudgment of atrial fibrillation for P peak absence.[51] The intensity of peaks was calculated by the difference value between the highest point and the baseline. As detailed in Table S3, the ratio of every peak of collected ECG was calculated separately. After removing the maximum and minimum values, the mean values of calculated P/R ratios of medical gel, Au@Ni mesh, and mesh e-tattoo electrodes were ∼0.219, ∼0.210, and ∼0.218, respectively. The mesh e-tattoo demonstrated a stronger ECG peak value and a very close P/R ratio compared with the performances of commercial medical gel, revealing the suitability and reliability of the mesh e-tattoo in ECG signal recording.

In particular, the EOG is commonly used to monitor eye movements by analyzing the electrical potential variation of facial skin surrounding the eyes. The generation of EOG signals is based on the principle depicted in Figure 6A. Typically, a potential difference arises between the cornea and retina due to the hyperpolarization and depolarization of ions across the cell membrane.[52] The cornea exhibits a positive charge, and the retina displays a negative one. This potential difference builds an electrical dipole along the cornea/retina axis. When the eyes move, the dipole rotates simultaneously, changing the potential gradient of the surrounding eye regions correlated with the level of the eye rotation angle. The potential can be either positive or negative depending on the position of the reference electrode. The reference electrode was put on the central part of the forehead. As a result, a straight potential baseline is detected when gazing straight ahead without eye movement. If the eyes move to the left, an electrical potential peak appears, while a signal valley is to be expected if the eyes move to the right.

Five mesh e-tattoos were adhered to the forehead region of a volunteer to implicate EOG signals to HCI applications, as shown in Figure 6B. A reference electrode and a ground e-tattoo electrode were attached vertically in the middle of the forehead, and the other three e-tattoos, which acted as working electrodes, were adhered to the left, middle, and right sides in a triangle-shaped distribution around the forehead. Channel 2 was aligned with the reference electrode in the same vertical plane, while channels 1 and 3 occupied the same horizontal plane. Consequently, channel 2 functioned as a horizontal reference channel for left−right eye movements, serving as a control group for channels 1 and 3. Its significance stems from providing a more intuitive visualization of signal variations during horizontal eye movements. For practical applications, we focused exclusively on the horizontal eye movements captured by channels 1 and 3, ensuring accuracy and feasibility. Channel 2 remains reserved for potential future use as a control channel for vertical eye movements in subsequent work. The EOG measurements were conducted using a wireless EEG acquisition system that could be fixed to the arm and did not interfere with body activities (Figure S18 and Movie S1). The volunteer was asked to periodically "look right" and "look left" several times while the data were recorded in real time.

Any interference signals from EEG, ECG, or environmental affection must be filtered out in order to obtain an accurate waveform. Therefore, we first used a bandpass filter with a range of 0.5−100 Hz to suppress the noise level, which is typical for EEG data processing. A 6 s section of EEG signal that included consecutive "look left" and "look right" movements was analyzed. The results obtained revealed that the change in the amplitude consistently corresponded to the events under test (Figure 6C). In the next step, the signaling segments were further investigated by Fourier transform (FFT) analysis and optimized within the low-frequency range bandpass filter (0.5−10 Hz) to boost the real-time data processing efficiency and speed (Figure 6D). The detailed data processing and optimizing method are provided in the Supporting Information. The resulting signal waveforms were relatively smooth, and noticeable positive and negative peaks could be identified by comparing the signals of "blink", "look left", and "look right" (Figure S19). Based on the geometrical arrangement of the e-tattoo sensors, the two channels positioned above the left and right eyes exhibited opposing responses during left and right eye movements. For example, the eye movement of "look left" delivered a positive signal peak in the left channel and a negative signal valley in the right channel at the same moment. By establishing appropriate thresholds and criteria, we successfully identified typical eye movements, such as left-ward gaze, right-ward gaze, and blinking, in real time.

The implementation of the algorithm in virtual reality (VR) scene control allows users to manipulate and interact with the virtual environment, enhancing the immersive experience and providing a novel means of interaction. We developed a real-time EOG signal processing algorithm for recording and identifying the typical EOG feature obtained by the mesh e-tattoo to control a VR object on a computer screen wirelessly. The performance evaluation of the developed system involved analyzing offline data collected from a series of participants and subsequent real-time data analysis. Three types of user actions were defined in our VR application: rotating, moving the target object, and rotating the user's perspective. Within the scenario, a user interface (UI) allows the user to switch between different types of actions.

The types of actions that the UI can manipulate include the following functions: moving the target object: "look left" moves the target object to the left of the user's perspective, and "look right" moves it to the right (Figure 6E,F and Movie S2). Rotating the target object: "look left" rotates the target object clockwise on the horizontal plane, and "look right" rotates it counterclockwise (Movie S3). Rotating the user's perspective: "look left" rotates the user's perspective counterclockwise on the horizontal plane, simulating the left turn of the human head, and "look right" rotates clockwise, simulating the right turn (Movie S4). Our experiment aimed to enhance the user experience by ensuring the alignment of the volunteer's eye movement direction with the movement direction of the

https://doi.org/10.1021/acsami.5c00565
ACS Appl. Mater. Interfaces 2025, 17, 22337−22351

virtual object in VR (Figure S20). This synchronization aimed to create more immersive and intuitive interactions for the user. We performed a VR-controlling experiment with the three modes, demonstrating the signal collection and HCI by the mesh e-tattoo successfully. Compared with previous HCI works of controlling a robot hand,[53] driving prosthetic fingers,[54] or controlling a small game in MATLAB[55] by EMG produced from muscle activities, our work realized VR application using EOG instructional signals collected with transparent mesh e-tattoos, integrating high-quality bioelectrical signal detection, wireless data transferring, real-time signal data analyzing, and simultaneous VR object control. The HCI demonstration revealed the superiority of the mesh e-tattoo in the extraction of signals and the applicability of spontaneous eye movements for interface control, which indicated great potential in VR or artificial reality (AR) controlling applications.

3. CONCLUSIONS

In summary, a highly transparent and fully breathable freestanding flexible mesh e-tattoo has been successfully developed for bioelectrical signal detection. Its exceptional properties are attributed to its flexible and deformation-tolerant structure that comprises a conductive metal mesh skeleton integrated with a biocompatible soft conductive polymer shell. The capillary-driven meniscus force exerted by the mesh tattoo featuring a boosted liquid bridge number is stronger than the force generated by a compact electrode covering the entire surface. This enhanced adhesion force, particularly in sweaty conditions, is a significant advantage offered by the mesh design. The carved mesh provides a seamless and adaptive fit on the skin and aids in adhesion due to the boost in meniscus force. The mesh design also improves water evaporation, enhancing the adhesive properties. The e-tattoo exhibited a visible-light transmittance of 95%, and the sheet resistance was as low as ~0.268 Ω sq^{-1}, corresponding to an impressive FoM of up to $2.7 \times 10.^4$ The mesh e-tattoo seamlessly attached to the skin ensures unobstructed airflow and high optical clarity, making it an ideal candidate for long-term wearable electrodes for bioelectrical signal monitoring. The mesh e-tattoo demonstrated remarkable durability against repeated mechanical folding and stretching. According to the stretching-to-fracture tests, mesh e-tattoos showed a broad tensile range with a small Young's modulus, which was much lower than that of human skin. During the detection of bioelectrical signals, the mesh e-tattoo exhibited decent contact with the skin. Stable signals with low noise could be collected at a similar level to that of commercial medical gel electrodes. To sum up, the freestanding mesh e-tattoo exhibits excellent breathability and transparency while maintaining superior conductivity and compatibility with the skin. These unique advantages position it as a cutting-edge wearable device for daily monitoring of skin bioelectrical signals, promising significant development in the field of HCI applications. The robust electronic properties and shape adaptability further enhance its practical utility in various monitoring scenarios. As such, the mesh e-tattoo represents a significant step forward in the evolution of wearable technology and holds great potential for future advancements in healthcare, fitness tracking, and beyond.

4. EXPERIMENTAL SECTION

Design of the Mesh Structure and Mold Fabrication. The mesh pattern (~14 mm × 14 mm) was designed by Ledit 11.1 software with a 15 μm line width and four contact points (2 mm diameter) consisting of grids with a width of 20 μm. The curve mesh was designed with eight vertical lines and eight parallel lines, where the distance between lines was 2 mm. Through direct laser writing (Microlab-4, SVG Tech), the pattern was exported and formed on a chrome (Cr) plate coated with photoresist AZ1500 (500 nm). After developing in the TMAH (tetramethylammonium hydroxide, 2.38%, ZX-238) developer for 8 s, the pattern emerged on the surface. Then, Cr was etched with an etchant for ~60 s, which was prepared by dispersing 200 g of ceric ammonium nitrate in 35 mL of acetic acid glacial and adding DI water to a volume of 1000 mL. The remaining photoresist was stripped with 5% NaOH solution. After the sample was washed with DI water and dried under nitrogen flow, a photolithography mask was fabricated.

ITO glass (2 cm × 2 cm) was chosen as the substrate. The surfaces were scrubbed with detergent and ultrasonically cleaned in acetone, DI water, and ethanol for 30 min, sequentially. Next, the substrates were dried under a nitrogen flow and activated by oxygen plasma (Harrick Plasma, PDC-002, HI) for 15 min. The cleaned substrate was spin-coated with OmniCoat (MicroChem) at 500 rpm for 15 s and 3000 rpm for 30 s and then baked at 200 °C (Lebo Science) for 1 min. After cooling to room temperature, the substrate with the OmniCoat layer was spin-coated with SU-8 3050 (negative photoresist, Microchem) at 500 rpm for 20 s and 4000 rpm for 30 s and then baked at 95 °C for ~15 min.

Photolithography was conducted with a Cr mask and SU-8-coated substrates with 7.7 s of exposure (SUSS MicroTec, MJB4, with a light intensity of 40 mW/cm^2). Then, the substrates were hard baked at 95 °C for 3 min and developed in PGMEA (propylene glycol methyl ether acetate, 99%, Aladdin) for 6 min. The samples were cleaned in DI water and dried with nitrogen. Finally, the substrates were subjected to oxygen plasma for 15 min to remove the remaining OmniCoat remnant at the bottom of the trench pattern.

Fabrication of the Freestanding Metal Mesh Structure. A source meter (Keithley 2612A) was used for electrodeposition. The ITO substrate was connected to the anode, and a Ni plate was connected to the cathode. The two poles were immersed in a nickel sulfate electroplating solution (Beichen). Then, a constant current of 6 mA was applied for 30 min, after which the Ni mesh was regenerated. After that, the substrate was washed with DI water and soaked in NMP (*N*-methylpyrrolidone, 98%, Aladdin) at 50 °C for 30 min, after which the resist was swollen and stripped, releasing the Ni mesh.

The Ni mesh was fixed by a copper wire and immersed in a Au electroplating solution (Beichen), which was connected to the anode, while a titanium wire was immersed as a cathode. The source meter applied a constant current of 3 mA on the path for 10 min. Abundant small bubbles appeared on the surface of the mesh as Au was covered. The mesh was subsequently washed with DI water and dried by nitrogen blowing.

Surface Modification and Electropolymerization of PEDOT. First, 0.1 g of PVA (124, Ourchem, GR) powder was stirred with 10 g of DI water for 1 h at 90 °C to form a 1% PVA solution. The Au-coated mesh was treated with oxygen plasma for 15 min and then incubated in 1 mM cysteamine solution[29] for 1 h to functionalize the mesh with amino groups. Next, the surface was coated with a PVA solution several times and heated at 80 °C for 30 min to ensure drying. The solution for electrochemical polymerization was composed of 0.01 M 3,4-ethylenedioxythiophene (3,4-EDOT) (Aladdin, 99%) and 0.1 M $LiClO_4$ (Aladdin, 99.9%) in DI water. When the mesh was dry, it was connected to the working electrode, a platinum sheet (1 cm × 1 cm) was used as the counter electrode, and a Ag/AgCl wire was used as the reference electrode. The reaction occurred at a constant voltage of 2 V for 2 min in an electrochemical workstation (CHI660E).

https://doi.org/10.1021/acsami.5c00565
ACS Appl. Mater. Interfaces 2025, 17, 22337−22351

Optical and Electrical Characterization. The transmittance of the mesh e-tattoo was measured by a UV-vis-NIR spectrophotometer (PerkinElmer, Lambda 1050+). The haze was measured by a UV-vis-NIR spectrophotometer (UV-3150 Shimadzu, Japan, LISR-3100). The infrared thermal images were taken by an infrared thermal imager (Hikvision, DS-2TPH10-3AUF). The Raman spectrum was measured by a Raman spectrometer (WITec, alpha300 R). SEM (ZEISS, G500) and 3D microscopy (Leica, DCM8) were employed to observe the surface morphology of samples.

Contact impedance was measured through a precision impedance analyzer (>100 Hz) (Wayne Kerr, 6500B) and electrochemical workstation (1−100 Hz) (CHI660E), using a medical gel reference electrode ∼10 cm away from the measured sample on human skin. The sheet resistance was attained by four-probe resistance tester (Suzhou Lattice Electronics, ST2258A).

Repeated Stretching, Bending, and Tension Limit Tests. The repeated stretching and bending tests were carried out by a mechanical cyclic deformation system for flexible electronics (Nanoupe, FlexTest-TM-L). The tattoo sample was adhered to rectangle Cu tapes at two sides and loaded at the fixture, where the mesh part remained ∼8 mm in length. The system operated with a constant rate of 0.5 mm/s for the stretching mode and 1 °/s for the bending mode. The resistance was measured by a Keithley 2612A source meter in real time by clamping the electrodes at the Cu tapes bilaterally.

The tension limit test was carried out by universal testing systems (Instron, 34TM-50). The mesh e-tattoo was fixed by Cu tape at two sides and loaded between fixtures by small clamps. In the three-point bending test, the displacement that remained between tapes was ∼8 mm. The operation rate was 0.5 mm/s, and the finished operation after the sample broke completely.

Real-Time EOG Signal Detection and Human−Computer Interactions. The mesh e-tattoo was electrically connected to a wireless BCI amplifier (Neuracle NeuSen W) by bonding enameled copper wires to the round contact points at the corners of the e-tattoos to acquire signals from the mesh e-tattoo. The communication between the laptop and the wireless amplifier utilized a local area network for data transmission.

Another laptop was used for the VR control. The two laptops communicated with each other using TCP/IP. This setup allowed for the real-time acquisition and analysis of EOG signals using the wireless EEG amplifier system and mesh e-tattoo as well as the integration of these signals into a VR environment for user control.

In addition, volunteers were recruited for this study and signed a written informed consent before the experiment began. All of the experiments were approved by the Ethics Committee of Tsinghua University and were implicated by relevant guidelines and regulations. The volunteers took part in the experiment to control the VR platform with their consent. They reported healthy neurological, psychological, and skin conditions. The forehead of the volunteer was wiped with 75% medical alcohol cotton pads before the electrodes were fixed. Although decent signals could be obtained, medical conductive paste (Greentek) was applied when applying HCI demonstration to assist in attachment, where the impedance could be as low as ∼10 kΩ (Figure S21).

During the experiments, the volunteer was asked to sit comfortably in front of a monitor with his face parallel to the screen and his brow aligned with the screen center. In the process, three channels were used for data acquisition with both the ground electrode and the reference electrode attached to the forehead. The enameled copper wires were fixed on the forehead by some transparent tapes. These procedures were implemented to ensure the volunteer's safety, comfort, and adherence to standard protocols for collecting reliable data for the study.

■ ASSOCIATED CONTENT

Supporting Information

The Supporting Information is available free of charge at https://pubs.acs.org/doi/10.1021/acsami.5c00565.

Description of data processing and human−computer interaction, MATLAB code of choosing the signal segment, filtering, STFT and FFT analysis, and electrodeposition reaction equations on sample; sketch diagram of the metal mesh structure; pictures of contact angles on PEDOT/Au/Ni and skin surfaces; schematic of a 2R × 2R flat surface with single meniscus and $N = n \times n$ menisci; diagram of the mesh e-tattoo fabrication process; EOG signal collected by the Cu@Ni mesh electrode; SEM and EDS images of Ni mesh coated with a thinner Au layer of ∼50 nm; average resistance-bending angle plot of the repeated bending test; photographs of the mesh e-tattoo when stretching to 100% in repeated tests and in the process of the force−displacement test; light transmittance spectra of metal skeletons with different grid densities; haze curve of mesh e-tattoos; impedance−frequency plots for samples of the mesh e-tattoo, Au@Ni mesh, and medical gel attached to human skin in the frequency range between 1 and 100 Hz; diagram of PEDOT attached onto skin; impedance variation of the mesh e-tattoo on pig skin for 7-day continuous measurement and impedance change of medical gel electrode and mesh e-tattoo on pig skin in 8 h; contact impedance and skin conditions before and after 12 h wearing test; photographs of skin surface after attaching the mesh e-tattoo and medical gel; images of topography, 3D height, and cross-section profile of the mesh e-tattoo attaching on pig skin; photographs of the forehead of the volunteer with the mesh tattoo attached when wrinkling and relaxing eyebrow; waveforms of three channels for blink, look left, and look right in the 0.5−10 Hz filtering range; real-time digital photograph of the controlling VR object by the volunteer; real-time impedance values during detection with conductive paste; table of stability of TCE under mechanical deformation conditions; table of the SNRs and baseline noise of medical gel, Au@Ni mesh, and mesh e-tattoo for EMG, ECG, and EOG; and table of the values of P, R, and P/R ratio for 13 peaks of ECGs and the mean value of medical gel, Au@Ni mesh, and mesh e-tattoo (PDF)

Movie of a data collection process of a walking volunteer wearing wireless EEG system (MP4)

Movie of the process of moving the target object by the horizontal movement of eyes (MP4)

Movie of the process of rotating the target object by the horizontal movement of eyes (MP4)

Movie of the process of rotating the user's perspective by the horizontal movement of eyes (MP4)

■ AUTHOR INFORMATION

Corresponding Authors

Tao Song − *Institute of Functional Nano & Soft Materials (FUNSOM), Jiangsu Key Laboratory for Carbon-Based Functional Materials & Devices, Soochow University, Suzhou, Jiangsu 215123, P. R. China;* orcid.org/0000-0002-2978-8829; Email: tsong@suda.edu.cn

Weihua Pei − *Laboratory of Solid State Optoelectronics Information Technology, Institute of Semiconductors, Chinese Academy of Sciences, Beijing 100083, P. R. China;* Email: peiwh@semi.ac.cn

Baoquan Sun − *Institute of Functional Nano & Soft Materials (FUNSOM), Jiangsu Key Laboratory for Carbon-Based Functional Materials & Devices, Soochow University, Suzhou, Jiangsu 215123, P. R. China; Macau Institute of Materials Science and Engineering, MUST-SUDA Joint Research Center for Advanced Functional Materials, Macau University of Science and Technology, Macau 999078, P. R. China;* orcid.org/0000-0002-4507-4578; Email: bqsun@suda.edu.cn

Authors

Xiang Li − *Institute of Functional Nano & Soft Materials (FUNSOM), Jiangsu Key Laboratory for Carbon-Based Functional Materials & Devices, Soochow University, Suzhou, Jiangsu 215123, P. R. China*

Junyi Zhang − *School of Advanced Technology, Xi'an Jiaotong-Liverpool University, Suzhou, Jiangsu 215123, P. R. China*

Bo Shi − *Institute of Functional Nano & Soft Materials (FUNSOM), Jiangsu Key Laboratory for Carbon-Based Functional Materials & Devices, Soochow University, Suzhou, Jiangsu 215123, P. R. China*

Yawen Li − *Institute of Functional Nano & Soft Materials (FUNSOM), Jiangsu Key Laboratory for Carbon-Based Functional Materials & Devices, Soochow University, Suzhou, Jiangsu 215123, P. R. China*

Yanan Wang − *Institute of Functional Nano & Soft Materials (FUNSOM), Jiangsu Key Laboratory for Carbon-Based Functional Materials & Devices, Soochow University, Suzhou, Jiangsu 215123, P. R. China*

Kexiang Shuai − *School of Advanced Technology, Xi'an Jiaotong-Liverpool University, Suzhou, Jiangsu 215123, P. R. China*

Yue Li − *School of Advanced Technology, Xi'an Jiaotong-Liverpool University, Suzhou, Jiangsu 215123, P. R. China*

Gege Ming − *Department of Biomedical Engineering, Tsinghua University, Beijing 100084, P. R. China*

Complete contact information is available at: https://pubs.acs.org/10.1021/acsami.5c00565

Author Contributions

[§]X.L. and J.Z. contributed equally to this work.

Author Contributions

X.L.: investigation, fabrication, and characterization of the mesh e-tattoo; formal analysis; signal detection; visualization; and writing—original draft. J.Z.: investigation; software; theoretical research of human−computer interaction; and validation. B.S.: data curation; FEA analysis; and human experiment volunteer. Y.L.: visualization and 3D modeling. Y.W.: validation and data curation. K.S.: software and code and algorithms. Y.L.: validation and supervision of the HCI experiment. G.M.: supervision of ethical standards. T.S.: methodology; supervision; and writing review and editing. W.P.: supervision; validation; and software. B.S.: conceptualization; supervision; funding acquisition; writing review and editing; and project administration. The manuscript was written through contributions of all authors. All authors have given approval to the final version of the manuscript.

Notes

The authors declare no competing financial interest.

■ ACKNOWLEDGMENTS

We would like to acknowledge the support provided by the National Natural Science Foundation of China (Grant No. 62274116), and the Jiangsu Provincial Departments of Science and Technology (Grant No. BE2022025). Additionally, we are grateful for the funding received from the 2024 China-France Hubert Curien Partnership Program-Cai Yuanpei Project through China International Science and Technology Cooperation (CFPHC2024006), the 111 Program, the Collaborative Innovation Center of Suzhou Nano Science and Technology, the Science and Technology Development Fund, Macau SAR (0017/2022/AGJ), and the Priority Academic Program Development of Jiangsu Higher Education Institutions. The Institution Review Board of Tsinghua University approved this study (No. 20230058).

■ REFERENCES

(1) Liao, L.-D.; Chen, C.-Y.; Wang, I.-J.; Chen, S.-F.; Li, S.-Y.; Chen, B.-W.; Chang, J.-Y.; Lin, C.-T. Gaming Control Using a Wearable and Wireless EEG-Based Brain-Computer Interface Device with Novel Dry Foam-Based Sensors. *J. Neuroeng. Rehabil.* **2012**, *9*, 5.

(2) Prashant, P.; Joshi, A.; Gandhi, V. Brain Computer Interface: A Review. In *2015 5th Nirma University International Conference on Engineering (NUiCONE)*; **2015**, 1-6.

(3) Mason, S. G.; Birch, G. E. A General Framework for Brain-Computer Interface Design. *IEEE Trans. Neural Syst. Rehabil. Eng.* **2003**, *11*, 70.

(4) Grimaldi, G.; Manto, M. Neurological Tremor: Sensors, Signal Processing and Emerging Applications. *Sensors* **2010**, *10*, 1399.

(5) Zhao, S.; Liu, J.; Gong, Z.; Lei, Y.; OuYang, X.; Chan, C. C.; Ruan, S. Wearable Physiological Monitoring System Based on Electrocardiography and Electromyography for Upper Limb Rehabilitation Training. *Sensors* **2020**, *20*, 4861.

(6) Zhang, Y.; Fu, J.; Ding, Y.; Babar, A. A.; Song, X.; Chen, F.; Yu, X.; Zheng, Z. Thermal and Moisture Managing E-Textiles Enabled by Janus Hierarchical Gradient Honeycombs. *Adv. Mater.* **2024**, *36*, No. 2311633.

(7) Liu, Z.; Qi, D.; Hu, G.; Wang, H.; Jiang, Y.; Chen, G.; Luo, Y.; Loh, X. J.; Liedberg, B.; Chen, X. Surface Strain Redistribution on Structured Microfibers to Enhance Sensitivity of Fiber-Shaped Stretchable Strain Sensors. *Adv. Mater.* **2018**, *30*, No. 1704229.

(8) Yang, B.; Xiong, Y.; Ma, K.; Liu, S.; Tao, X. Recent Advances in Wearable Textile-Based Triboelectric Generator Systems for Energy Harvesting from Human Motion. *EcoMat* **2020**, *2*, No. e12054.

(9) Xue, J.; Zou, Y.; Deng, Y.; Li, Z. Bioinspired Sensor System for Health Care and Human-Machine Interaction. *EcoMat* **2022**, *4*, No. e12209.

(10) Chen, Y.-Y.; Lai, H.-Y.; Lin, S.-H.; Cho, C.-W.; Chao, W.-H.; Liao, C.-H.; Tsang, S.; Chen, Y.-F.; Lin, S.-Y. Design and Fabrication of a Polyimide-Based Microelectrode Array: Application in Neural Recording and Repeatable Electrolytic Lesion in Rat Brain. *J. Neurosci. Meth.* **2009**, *182*, 6.

(11) Schalk, G.; Miller, K. J.; Anderson, N. R.; Wilson, J. A.; Smyth, M. D.; Ojemann, J. G.; Moran, D. W.; Wolpaw, J. R.; Leuthardt, E. C. Two-Dimensional Movement Control Using Electrocorticographic Signals in Humans. *J. Neural Eng.* **2008**, *5*, 75.

(12) Chi, Y. M.; Jung, T.-P.; Cauwenberghs, G. Dry-Contact and Noncontact Biopotential Electrodes: Methodological Review. *IEEE Rev. Biomed. Eng.* **2010**, *3*, 106.

(13) Wang, X.; Gu, Y.; Xiong, Z.; Cui, Z.; Zhang, T. Silk-Molded Flexible, Ultrasensitive, and Highly Stable Electronic Skin for Monitoring Human Physiological Signals. *Adv. Mater.* **2014**, *26*, 1336.

(14) Zou, X.; Xue, J.; Li, X.; Chan, C. P. Y.; Li, Z.; Li, P.; Yang, Z.; Lai, K. W. C. High-Fidelity sEMG Signals Recorded by an on-Skin Electrode Based on AgNWs for Hand Gesture Classification Using Machine Learning. *ACS Appl. Mater. Interfaces* **2023**, *15*, 19374.

(15) Zhuang, Q.; Yao, K.; Zhang, C.; Song, X.; Zhou, J.; Zhang, Y.; Huang, Q.; Zhou, Y.; Yu, X.; Zheng, Z. Permeable, Three-Dimensional Integrated Electronic Skins with Stretchable Hybrid Liquid Metal Solders. *Nat. Electron.* **2024**, *7*, 598.
(16) Wang, S.; Cheng, H.; Yao, B.; He, H.; Zhang, L.; Yue, S.; Wang, Z.; Ouyang, J. Self-Adhesive, Stretchable, Biocompatible, and Conductive Nonvolatile Eutectogels as Wearable Conformal Strain and Pressure Sensors and Biopotential Electrodes for Precise Health Monitoring. *ACS Appl. Mater. Interfaces* **2021**, *13*, 20735.
(17) Lee, G.-H.; Moon, H.; Kim, H.; Lee, G. H.; Kwon, W.; Yoo, S.; Myung, D.; Yun, S. H.; Bao, Z.; Hahn, S. K. Multifunctional Materials for Implantable and Wearable Photonic Healthcare Devices. *Nat. Rev. Mater.* **2020**, *5*, 149.
(18) Inzelberg, L.; Rand, D.; Steinberg, S.; David-Pur, M.; Hanein, Y. A Wearable High-Resolution Facial Electromyography for Long Term Recordings in Freely Behaving Humans. *Sci. Rep.* **2018**, *8*, 2058.
(19) Rogers, J. A.; Someya, T.; Huang, Y. Materials and Mechanics for Stretchable Electronics. *Science* **2010**, *327*, 1603.
(20) Tang, L.; Shang, J.; Jiang, X. Multilayered Electronic Transfer Tattoo That Can Enable the Crease Amplification Effect. *Sci. Adv.* **2021**, *7*, No. eabe3778.
(21) Gogurla, N.; Kim, Y.; Cho, S.; Kim, J.; Kim, S. Multifunctional and Ultrathin Electronic Tattoo for On-Skin Diagnostic and Therapeutic Applications. *Adv. Mater.* **2021**, *33*, No. 2008308.
(22) Wang, Z.; Zhou, Z.; Li, C.; Liu, X.; Zhang, Y.; Pei, M.; Zhou, Z.; Cui, D.; Hu, D.; Chen, F.; Cao, W. A Single Electronic Tattoo for Multisensory Integration. *Small Methods* **2023**, *7*, No. 2201566.
(23) Kabiri Ameri, S.; Ho, R.; Jang, H.; Tao, L.; Wang, Y.; Wang, L.; Schnyer, D. M.; Akinwande, D.; Lu, N. Graphene Electronic Tattoo Sensors. *ACS Nano* **2017**, *11*, 7634.
(24) Lee, G.; Woo, H.; Yoon, C.; Yang, C.; Bae, J.; Kim, W.; Lee, D. H.; Kang, H.; Han, S.; Kang, S.; Park, S.; Kim, H.; Jeong, J.; Park, S. A Personalized Electronic Tattoo for Healthcare Realized by On-the-Spot Assembly of an Intrinsically Conductive and Durable Liquid-Metal Composite. *Adv. Mater.* **2022**, *34*, No. 2204159.
(25) Zhang, S.; Ling, H.; Chen, Y.; Cui, Q.; Ni, J.; Wang, X.; Hartel, M. C.; Meng, X.; Lee, K.; Lee, J.; Sun, W.; Lin, H.; Emaminejad, S.; Ahadian, S.; Ashammakhi, N.; Dokmeci, M. R.; Khademhosseini, A. Hydrogel-Enabled Transfer-Printing of Conducting Polymer Films for Soft Organic Bioelectronics. *Adv. Funct. Mater.* **2020**, *30*, No. 1906016.
(26) Byun, S.-H.; Sim, J. Y.; Zhou, Z.; Lee, J.; Qazi, R.; Walicki, M. C.; Parker, K. E.; Haney, M. P.; Choi, S. H.; Shon, A.; Gereau, G. B.; Bilbily, J.; Li, S.; Liu, Y.; Yeo, W.-H.; McCall, J. G.; Xiao, J.; Jeong, J.-W. Mechanically Transformative Electronics, Sensors, and Implantable Devices. *Sci. Adv.* **2019**, *5*, No. eaay0418.
(27) Huber, G.; Mantz, H.; Spolenak, R.; Mecke, K.; Jacobs, K.; Gorb, S. N.; Arzt, E. Evidence for Capillarity Contributions to Gecko Adhesion from Single Spatula Nanomechanical Measurements. *P. Natl. Acad. Sci.* **2005**, *102*, 16293.
(28) Cai, S.; Bhushan, B. Meniscus and Viscous Forces during Separation of Hydrophilic and Hydrophobic Smooth/Rough Surfaces with Symmetric and Asymmetric Contact Angles. *Philos. Trans. R. Soc. A* **2008**, *366*, 1627.
(29) Inoue, A.; Yuk, H.; Lu, B.; Zhao, X. Strong Adhesion of Wet Conducting Polymers on Diverse Substrates. *Sci. Adv.* **2020**, *6*, No. eaay5394.
(30) Xue, Y.; Chen, X.; Wang, F.; Lin, J.; Liu, J. Mechanically-compliant Bioelectronic Interfaces through Fatigue-resistant Conducting Polymer Hydrogel Coating. *Adv. Mater.* **2023**, *35*, No. 2304095.
(31) Mathur, P.; Raman, S. Electromagnetic Interference (EMI): Measurement and Reduction Techniques. *J. Electron. Mater.* **2020**, *49*, 2975.
(32) Nešpůrek, S.; Kuberský, P.; Polanský, R.; Trchová, M.; Šebera, J.; Sychrovský, V. Raman Spectroscopy and DFT Calculations of PEDOT:PSS in a Dipolar Field. *Phys. Chem. Chem. Phys.* **2021**, *24*, 541.
(33) Cui, N.; Song, Y.; Tan, C.-H.; Zhang, K.; Yang, X.; Dong, S.; Xie, B.; Huang, F. Stretchable transparent electrodes for conformable wearable organic photovoltaic devices. *npj Flexible Electron.* **2021**, *5*, 31.
(34) Chen, X.; Yin, Y.; Yuan, W.; Nie, S.; Lin, Y.; Guo, W.; Su, W.; Li, Y.; Yang, K.; Cui, Z. Transparent Thermotherapeutic Skin Patch Based on Highly Conductive and Stretchable Copper Mesh Heater. *Adv. Electron. Mater.* **2021**, *7*, No. 2100611.
(35) Wu, H.; Yang, G.; Zhu, K.; Liu, S.; Guo, W.; Jiang, Z.; Li, Z. Materials, Devices, and Systems of On-Skin Electrodes for Electrophysiological Monitoring and Human−Machine Interfaces. *Adv. Sci.* **2021**, *8*, No. 2001938.
(36) Gueye, M. N.; Carella, A.; Demadrille, R.; Simonato, J.-P. All-Polymeric Flexible Transparent Heaters. *ACS Appl. Mater. Interfaces* **2017**, *9*, 27250.
(37) Khan, A.; Lee, S.; Jang, T.; Xiong, Z.; Zhang, C.; Tang, J.; Guo, L. J.; Li, W.-D. High-Performance Flexible Transparent Electrode with an Embedded Metal Mesh Fabricated by Cost-Effective Solution Process. *Small* **2016**, *12*, 3021.
(38) Wang, J.; Jiu, J.; Araki, T.; Nogi, M.; Sugahara, T.; Nagao, S.; Koga, H.; He, P.; Suganuma, K. Silver Nanowire Electrodes: Conductivity Improvement Without Post-Treatment and Application in Capacitive Pressure Sensors. *Nano-Micro Lett.* **2015**, *7*, 51.
(39) Zhang, G.; Liu, X.; Liu, H.; Wang, X.; Duan, F.; Yu, H.; Nie, Z.; Wei, D.; Zhang, Y.; Pan, H.; Duan, H. Customizable Metal Micromesh Electrode Enabling Flexible Transparent Zn-Ion Hybrid Supercapacitors with High Energy Density. *Small Methods* **2023**, *8*, No. 2300792.
(40) Infante, D.; Koch, K. W.; Mazumder, P.; Tian, L.; Carrilero, A.; Tulli, D.; Baker, D.; Pruneri, V. Durable, Superhydrophobic, Antireflection, and Low Haze Glass Surfaces Using Scalable Metal Dewetting Nanostructuring. *Nano Res.* **2013**, *6*, 429.
(41) Kouhsari, S. M., Ed. *Fundamental Research in Electrical Engineering: The Selected Papers of The First International Conference on Fundamental Research in Electrical Engineering*. Lecture Notes in Electrical Engineering; Singapore: Springer Singapore, 2019; Vol. *480*.
(42) Tian, F.; Yu, J.; Wang, W.; Zhao, D.; Cao, J.; Zhao, Q.; Wang, F.; Yang, H.; Wu, Z.; Xu, J.; Lu, B. Design of Adhesive Conducting PEDOT-MeOH:PSS/PDA Neural Interface via Electropolymerization for Ultrasmall Implantable Neural Microelectrodes. *J. Colloid Interface Sci.* **2023**, *638*, 339.
(43) Kim, R.; Nam, Y. Polydopamine-Doped Conductive Polymer Microelectrodes for Neural Recording and Stimulation. *J. Neurosci. Meth.* **2019**, *326*, No. 108369.
(44) Lu, Y.; Wen, Y.; Lu, B.; Duan, X.; Xu, J.; Zhang, L.; Huang, Y. Electrosynthesis and Characterization of Poly(Hydroxy-Methylated-3,4-Ethylenedioxythiophene) Film in Aqueous Micellar Solution and Its Biosensing Application. *Chin. J. Polym. Sci.* **2012**, *30*, 824.
(45) Donahue, M. J.; Sanchez-Sanchez, A.; Inal, S.; Qu, J.; Owens, R. M.; Mecerreyes, D.; Malliaras, G. G.; Martin, D. C. Tailoring PEDOT Properties for Applications in Bioelectronics. *Mater. Sci. Eng. R* **2020**, *140*, No. 100546.
(46) Berggren, M.; Malliaras, G. G. How Conducting Polymer Electrodes Operate. *Science* **2019**, *364*, 233.
(47) Chen, X.; Nie, S.; Guo, W.; Fei, F.; Su, W.; Gu, W.; Cui, Z. Printable High-Aspect Ratio and High-Resolution Cu Grid Flexible Transparent Conductive Film with Figure of Merit over 80000. *Adv. Electron. Mater.* **2019**, *5*, No. 1800991.
(48) Bel Hadj Tahar, R.; Ban, T.; Ohya, Y.; Takahashi, Y. Tin Doped Indium Oxide Thin Films: Electrical Properties. *J. Appl. Phys.* **1998**, *83*, 2631.
(49) Grosse, P.; Cassidy, M. J.; Brown, P. EEG−EMG, MEG−EMG and EMG−EMG Frequency Analysis: Physiological Principles and Clinical Applications. *Clin. Neurophysiol.* **2002**, *113*, 1523.
(50) Nawrocki, R. A.; Jin, H.; Lee, S.; Yokota, T.; Sekino, M.; Someya, T. Self-Adhesive and Ultra-Conformable, Sub-300 Nm Dry Thin-Film Electrodes for Surface Monitoring of Biopotentials. *Adv. Funct. Mater.* **2018**, *28*, No. 1803279.

(51) He, K.; Liu, Z.; Wan, C.; Jiang, Y.; Wang, T.; Wang, M.; Zhang, F.; Liu, Y.; Pan, L.; Xiao, M.; Yang, H.; Chen, X. An On-Skin Electrode with Anti-Epidermal-Surface-Lipid Function Based on a Zwitterionic Polymer Brush. *Adv. Mater.* **2020**, *32*, No. 2001130.
(52) Fang, C.; He, B.; Wang, Y.; Cao, J.; Gao, S. EMG-Centered Multisensory Based Technologies for Pattern Recognition in Rehabilitation: State of the Art and Challenges. *Biosensors* **2020**, *10*, 85.
(53) Zhao, Y.; Zhang, S.; Yu, T.; Zhang, Y.; Ye, G.; Cui, H.; He, C.; Jiang, W.; Zhai, Y.; Lu, C.; Gu, X.; Liu, N. Ultra-Conformal Skin Electrodes with Synergistically Enhanced Conductivity for Long-Time and Low-Motion Artifact Epidermal Electrophysiology. *Nat. Commun.* **2021**, *12*, 4880.
(54) Pan, L.; Cai, P.; Mei, L.; Cheng, Y.; Zeng, Y.; Wang, M.; Wang, T.; Jiang, Y.; Ji, B.; Li, D.; Chen, X. A Compliant Ionic Adhesive Electrode with Ultralow Bioelectronic Impedance. *Adv. Mater.* **2020**, *32*, No. 2003723.
(55) Guo, H.; Wang, H.; Xiang, Z.; Wu, H.; Wan, J.; Xu, C.; Chen, H.; Han, M.; Zhang, H. Soft Human−Machine Interface with Triboelectric Patterns and Archimedes Spiral Electrodes for Enhanced Motion Detection. *Adv. Funct. Mater.* **2021**, *31*, No. 2103075.

https://doi.org/10.1021/acsami.5c00565
ACS Appl. Mater. Interfaces 2025, 17, 22337−22351